# FLORE
# Repository istituzionale dell'Università degli Studi di Firenze

## High frame rate tri-plane echocardiography with spiral arrays: from simulation to real-time implementation

(Article begins on next page)

18 November 2024

# High frame rate tri-plane echocardiography with spiral arrays: from simulation to real-time implementation

Alessandro Ramalli, Sevan Harput, Stéphanie Bézy, Enrico Boni, Robert J. Eckersley, Piero Tortoli, and Jan D'hooge

*Abstract*— **Major cardiovascular diseases are associated with (regional) dysfunction of the left ventricle. Despite the 3D nature of the heart and its dynamics, the assessment of myocardial function is still largely based on 2D ultrasound imaging thereby making diagnosis heavily susceptible to the operator's expertise. Unfortunately, to date, 3D echocardiography cannot provide an adequate spatio-temporal resolution in real-time. Hence, tri-plane imaging has been introduced as a compromise between 2D and true volumetric ultrasound imaging. However, tri-plane imaging typically requires high-end ultrasound systems equipped with fully populated matrix array probes embedded with expensive and little flexible electronics for two-stage beamforming. This paper presents an advanced ultrasound system for real-time, high frame rate, tri-plane echocardiography based on low element count sparse arrays, i.e. the so-called spiral arrays. The system was simulated, experimentally validated, and implemented for real-time operation on the ULA-OP 256 system. Five different array configurations were tested together with four different scan sequences, including multi-line and planar diverging wave transmission. In particular, the former can be exploited to achieve, in tri-plane imaging, the same temporal resolution currently used in clinical 2D echocardiography, at the expenses of contrast (−3.5dB) and signal-to-noise ratio (−8.7dB). On the other hand, the transmission of planar diverging waves boosts the frame rate up to 250 Hz, but further compromises contrast (−10.5dB), signal-to-noise ratio (−9.7dB), and lateral resolution (+46%). In conclusion, despite an unavoidable loss in image quality and sensitivity due to the limited number of elements, high frame rate tri-plane imaging with spiral arrays is shown to be feasible in real-time and may enable real-time functional analysis of all left ventricular segments of the heart.**

*Index Terms*—**Cardiac imaging, high frame rate imaging, 3D imaging, tri-plane echocardiography, multiline transmission, diverging waves, spiral arrays, sparse arrays, real-time.**

A. Ramalli and J. D'hooge are with the Laboratory of Cardiovascular Imaging and Dynamics, Department of Cardiovascular Sciences, KU Leuven, 3000 Leuven, Belgium.

S. Harput is with the Division of Electrical and Electronic Engineering, London South Bank University, London, SE1 0AA, UK and the Department of Bioengineering, Imperial College London, London, SW7 2AZ, UK.

Stéphanie Bézy is with the Department of Cardiovascular Science, Division of Cardiology, UZ Leuven, KU Leuven, 3000 Leuven, Belgium.

R. J. Eckersley is with the Biomedical Engineering Department, Division of Imaging Sciences, King's College London, SE1 7EH, London, UK.

E. Boni, P. Tortoli are with the Department of Information Engineering, University of Florence, 50139, Florence, Italy.

## I. INTRODUCTION

The annual statistics reports of the heart associations [1], [2] show that cardiovascular diseases (CVDs) remain the leading cause of mortality and a major cause of morbidity in the Western developed countries. Since major CVDs are associated with (regional) dysfunction of the left ventricle [3], its accurate assessment, in real-time, during the whole heart cycle is essential.

Among the cardiac imaging modalities, echocardiography takes the leading role because of bedside applicability, good temporal resolution, real-time character, low cost and absence of ionizing radiation. Current standard clinical care, despite the 3D nature of the heart, is still largely based on 2D ultrasound imaging. This makes diagnosis heavily susceptible to the operator's expertise. Nevertheless, even though 3D echocardiography has been introduced in flagship scanners of the most important ultrasound companies, its great potential remains unexpressed due to technological limitations [4]–[8]. Indeed, the conventional acquisition schemes based on a line-by-line scan, also called single-line transmission (SLT), or the approach were multiple lines are reconstructed in parallel [9], i.e. multi-line acquisition (MLA), do not provide the required spatio-temporal resolution for an adequate field-of-view, as needed for reliable and reproducible quantitative measurements. Even if recent studies, based on research scanners and 1024-element matrices, have shown preliminary results on the feasibility and the potential of 3D imaging with high temporal resolution [10]–[12], vendors introduced real-time bi- and tri-plane imaging as an intermediate solution between 2D and full volumetric 3D imaging. These imaging modes consist in the simultaneous imaging of 2 or 3 cross sections of the heart, i.e. the 2- and the 4-chamber apical views or 2-, 3-, and 4-chamber views respectively. Moreover, they have been shown to be reliable clinical tools, providing comparable results to conventional 2D imaging, while shortening the acquisition and examination time [13]–[17]. Nonetheless, since the region of interest is still scanned by SLT/MLA, these imaging modes still come at a compromised time resolution (i.e. <40 Hz), disabling more advanced image analysis such as speckle tracking. Although 2D high frame rate (HFR) imaging techniques are becoming more common [18]–[25], their adaptation for 3D and multi-plane HFR imaging is still impractical. Indeed, they require fully sampled matrix arrays with thousands of small elements which, ideally,

should be individually controlled. A solution to reduce the size of the problem is the so called micro-beamforming technique [26], [27]. It consists in splitting the beamforming process in two consecutive stages, the first of which is implemented in the probe by embedding application-specific integrated circuits (ASIC); however, it is expensive, complex and little flexible. A possible alternative consists in smartly reducing either the number of channels to drive the probe, as in row-column-addressed arrays [28]–[30], or the number of elements, as in sparse arrays [31]–[35].

The aim of this work was to develop a real-time system for HFR tri-plane echocardiography based on spiral arrays with low-element count. First, we designed five different sparse array configurations and estimated, by Field II simulations [36], [37], their performance in four HFR scan sequences. Then, a prototype probe, to test all above array configurations, was built. The probe was connected to a prototype research scanner, i.e. ULA-OP 256 [38], in order to experimentally validate the simulation findings. Finally, HFR tri-plane imaging was implemented and tested in real-time.

The paper is organized as follows: Section II reviews the basics of sparse arrays based on Fermat's spirals and presents the design of the "multi-configuration" sparse array. Moreover, the implemented scan sequences, simulation details and experimental setups, as well as the performance metrics, are presented. Section III shows simulation and experimental results that are finally discussed in Section IV. Section V concludes and introduces possible perspectives.

## II. MATERIALS & METHODS

### A. Spiral arrays

Spiral arrays were defined according to the method described in [34]. The deterministic, aperiodic and balanced positions of the active transducer elements guarantee uniform performance over the wide range of steering angles needed in cardiac ultrasound volumetric imaging. Specifically, the elements are positioned according to Fermat's spiral seeds with spatial density modulation. In a nutshell, the position of the $n$-th element is defined by the radial distance from the array center $r_n$ and the angle with respect to the abscissa axis $\theta_n$. The latter can be defined as follows:

$$\theta_n = n \cdot \alpha \qquad (1)$$

where $\alpha = \pi(\sqrt{5} - 1)$ is the so-called *Golden Angle*, i.e. the angle that divides a complete turn in a *Golden Ratio*. On the other hand, the radial position of each element $r_n \in [0, R_{ap}]$, where $R_{ap}$ is the aperture radius, is determined by a three-step algorithm:

1. A rotationally symmetric weighting window function $A(r)$, which guarantees the desired side-lobe-level is selected, e.g. rectangular window, Hann's window, Tukey's window, Blackman's window, etc.
2. The inner ($R_{n-1}$) and outer ($R_n$) radii of the annular rings, enclosing the $n$-th element, are evaluated by solving the following equation:

$$2\pi \int_{R_{n-1}}^{R_n} A(r)r \, dr = \frac{A_{eff}}{N} \qquad n \in [1, N] \qquad (2)$$

where $N$ is the number of elements of the array, $R_0$ is imposed to be equal to 0, and $A_{eff}$ is the effective aperture, defined as

$$A_{eff} = 2\pi \int_0^{R_{ap}} A(r)r \, dr \qquad (3)$$

3. The radial position of the $n$-th element, $r_n$, is evaluated according to:

$$2\pi \int_{R_{n-1}}^{r_n} A(r)r \, dr = \frac{A_{eff}}{2N} \qquad n \in [1, N] \qquad (4)$$

For additional details on the positioning procedure, please refer to [34].

### B. Probe layout definition

The layout of the active elements was designed based on the gridded layout of the 2D matrix array (Vermon S.A., Tours, France). It consists of 32 (x-axis) by 35 (y-axis) elements (3.7 MHz, 300 µm pitch, 70% bandwidth), but on the y-direction every ninth row is not connected. The total number of addressable elements is thus 1024. On this probe, two sparse array layouts, hereinafter referred as PA and PB, were designed; both were based on an ungridded, 10.4-mm-wide spiral with 256 seeds [34], whose density tapering was modulated according to a 50%-Tukey window (SA and SB in Fig. 1). Specifically, SB was slightly rotated with respect to SA and the rotation angle was set equal to the *Golden Angle*. Then, the elements belonging to PA were selected among those of the Vermon matrix array, by activating those elements whose position was closest to the ideal position of the elements of SA. Similarly, the elements belonging to PB were selected by activating those elements whose position was closest to the ideal position of the elements of SB, after excluding those that were already assigned to PA. The two layouts were connected to two connectors (model DLP 408, ITT Cannon, CA, USA). In this way, an approximation of a 256-element density tapered spiral array could be driven by a 256-channel system. Moreover, a 512-element dense array (PA+PB in Fig. 1) with Tukey density tapering could be driven by a 512-element system. Two prototypes of the so designed probe were built by Vermon: one for the Department of Bioengineering, Imperial College London; a second one for the Department of Information Engineering, University of Florence. Finally, as discussed in more detail later, two additional configurations could be tested, by using PA for transmission and PB for reception and vice versa.

### C. Scan sequences

Tri-plane B-mode images were reconstructed; the region of interest (ROI) was accordingly scanned through 3 planes/sectors that were positioned at rotational angles $\phi_p$ of 0°, 45° and 90° (see Fig. 2), considered as the approximate
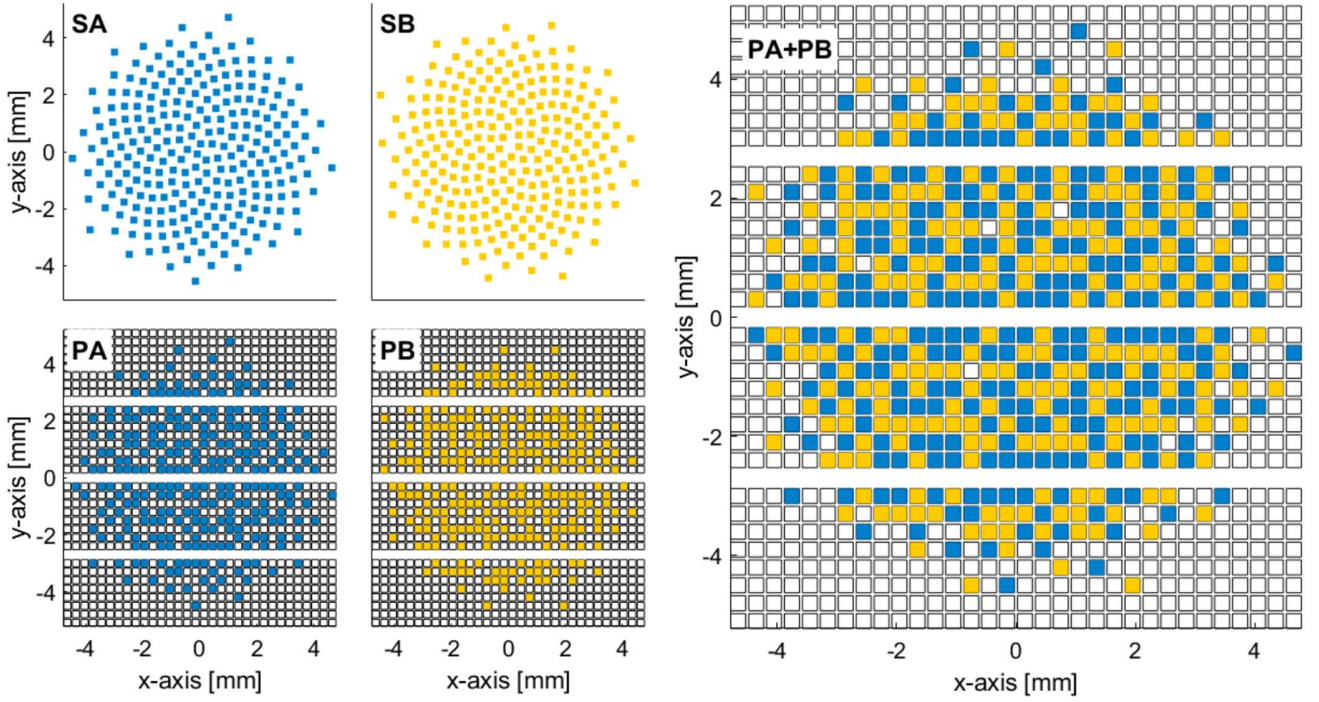
Fig. 1 Layout of the arrays. SA and SB: ungridded, 10.4-mm-wide spiral with 256 seeds, whose density tapering was modulated according to a 50%-Tukey window; they were the reference layouts to design PA and PB, i.e. the two gridded, sparse arrays whose elements were selected among those avaialble on the Vermon probe (its layout includes white, blue and yellow elements). PA+PB is the 512-element dense array that can be obtained by synchronizing two ULA-OP 256 systems to simultaneously drive PA and PB.

position of the apical 2-, 3-, and 4-chamber views [39] respectively. Moreover, four different scan sequences were tested: single-line transmission (SLT), multi-line transmission (MLT, [40]), single-plane transmission (SPT, [41]), and multi-plane transmission (MPT). Figure 3 and the related accompanying movie clip help in understanding how transmission events were designed and how they follow each other during the scan sequences.

SLT is the standard scan sequence, i.e. a focused beam scans the ROI line-by-line and plane-by-plane; for each beam position a single line is beamformed, so that the final frame rate results:

$$FR_{SLT} = \frac{PRF}{nL \cdot nP} \qquad (5)$$

where *PRF* is the pulse repetition frequency, *nP* is the number of scanned planes (in tri-plane imaging *nP*=3) and *nL* is the number of lines reconstructed for each of the planes (hereinafter *nL*=100).

For MLT imaging, *nMLT* beams were simultaneously transmitted; in this work, as in [42], each of the beams scanned only one out of the 3 reconstructed planes, hence *nMLT*=*nP*=3. Moreover, in order to limit the cross-talk among beams, an alternated pattern scheme was implemented as sketched in Fig. 4. In particular, for the i-th transmission event ($i \in [1, nL]$), the b-th beam ($b \in [1, nMLT]$) was transmitted along the image-plane line number

$$l_b(i) = 1 + \left\{ \left\lfloor \left\lfloor \frac{(b-1) \cdot nL}{nMLT} \right\rfloor + i - 1 \right\rfloor \% nL \right\} \qquad (6)$$

where $\lfloor \cdot \rfloor$ is the round to the closest integer operator and % is the modulus operator. Assuming a linear system, in order to simultaneously transmit *nMLT* beams into the $l_b(i)$ directions, the excitation waveform for a given element is given by the sum of the pulses, each properly delayed, that would be used on that element to generate conventional SLT beams along the $l_b(i)$ directions [43]. In tri-plane MLT imaging the theoretical final frame rate results:

$$FR_{MLT} = \frac{PRF \cdot nMLT}{nL \cdot nP}. \qquad (7)$$

In SPT imaging, a planar diverging wave is transmitted for every plane of interest on consecutive transmission events. In order to transmit planar diverging waves with a sparse array,
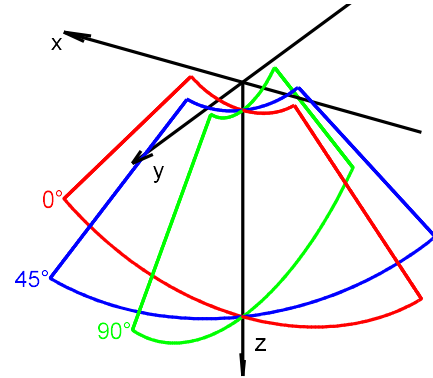


Fig. 2 The reference system and the reconstructed regions of interest. The probe is centered on the origin of the reference system. Tri-plane images are reconstructed at different rotational angles 0° (red), 90° (green) and 45° (blu), respectively.
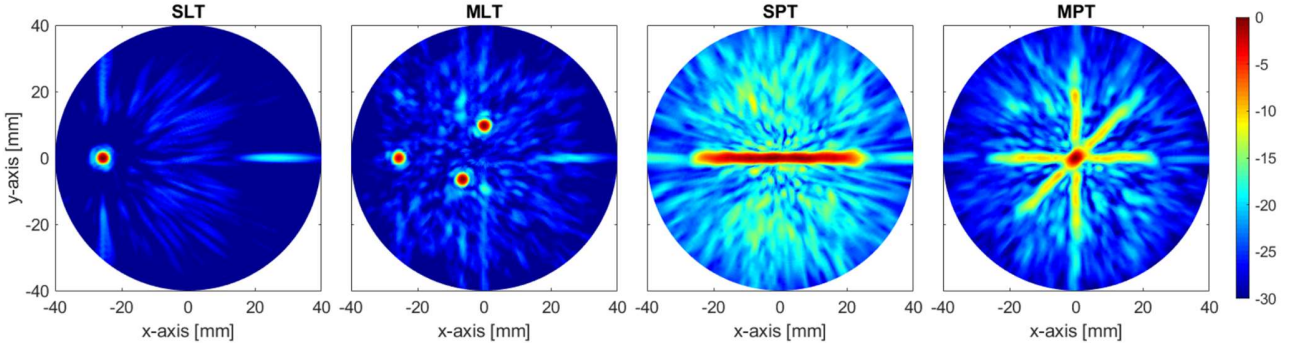
Fig. 3 Simulated one-way fields, radiated from the array configuration PA, for the first transmission event of each imaging mode. The fields were evaluated on the spherical cap having a 40 mm radius and were projected on the xy-plane. The simulated fields for the successive transmission events as a supplementary accompayning movie clip 🖥.

one needs to transmit a diverging wave, while, at the same time, focusing in the direction orthogonal to the rotational direction of the plane of interest [41]. In tri-plane SPT imaging, the theoretical final frame rate results:

$$FR_{SPT} = \frac{PRF}{nP}. \tag{8}$$

In MPT imaging, multiple planar diverging waves are simultaneously transmitted along the direction of the planes of interest. The approach is very similar to that of MLT imaging; however, instead of transmitting focused beams, planar diverging waves are transmitted. Hence, assuming a linear system, in order to simultaneously transmit $nP$ planar diverging waves into the $\phi_p$ planes, the excitation waveform for a given element is given by the sum of the pulses, each properly delayed, that would be used on that element to generate SPT diverging waves along the $\phi_p$ directions. In tri-plane MPT imaging the theoretical final frame rate results
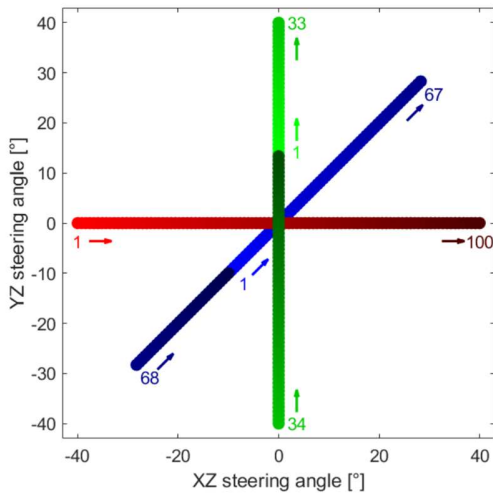
$$FR_{MPT} = PRF. \tag{9}$$



Fig. 4 Tri-plane alternated scan for the MLT sequence. Beam 1 (red), 2 (green), 3 (blue) respectively scan the planes at rotational angles 0°, 90° and 45°. Arrows indicate the scan direction; the numbers correspond to the transmission event index (n) for which the beams reach the borders of their respective scan plane. Moreover, "1s" highlight the position of the beams at the first transmission event.

It is worth highlighting that fully diverging waves, allowing full 3D HFR volume scan with a single transmission event, were not implemented since this work aimed at a real-time implementation, while reconstructing thousands of lines per transmission event is still far from being feasible in real-time in current ultrasound scanners.

### D. Simulation and experimental setup

#### 1) Array configurations

Given the availability of two 256-element sparse arrays connected to two independent systems, five different transmission/reception configurations were defined:

1) PA: the gridded sparse array PA is used both in transmission and in reception;
2) PB: the gridded sparse array PB is used both in transmission and in reception;
3) txPArxPB: PA is used in transmission, while PB is used in reception;
4) txPBrxPA: PB is used in transmission, while PA is used in reception;
5) PA+PB: arrays PA and PB are simultaneously and synchronously used both in transmission and in reception.

Hereinafter, PA and PB will be referred as single array configurations, txPArxPB and txPBrxPA as mixed configurations, while PA+PB as dense array.

#### 2) Transmission and reception settings

The basic transmitted signal was a 4-cycle, 3.7 MHz sine burst, tapered with a Hamming window, having a -6dB bandwidth of 1.7 MHz (46%). The opening sector angle for each scanned plane was set to 80°. In SLT and MLT, the transmission focal distance was set to 40 mm. In SPT and MPT, the virtual source position of diverging waves was set to (0, 0, -6) mm, to obtain a -10dB opening angle of about 80°; the focusing distance in the orthogonal direction to the plane scanned by the diverging wave was set to 40 mm. Given the density tapering of the transducer elements, apodization was implemented neither in transmission nor in reception.

#### 3) Simulations

Simulations were carried out in Matlab (The MathWorks,

Natick, MA) by using Field II. Two numeric phantoms were developed. The first, consisted of 4 point-scatterers in water, placed on the axis of the probe at 30, 40, 50, 60 mm depth, respectively, and was exploited to assess the system point spread functions (PSFs) at different depths. The second phantom consisted of a background tissue with randomly placed scatterers with a Gaussian scattering amplitude distribution and homogeneous spatial density distribution of 1,000 scatterers per cm$^3$. The phantom was centered at a depth of 40 mm, had a size of 80×80×30 mm$^3$, respectively along x, y, and z. Furthermore, a 10-mm-diameter anechoic cyst was centered at (0, 0, 40) mm to assess the image contrast performance.

*4) Experiments*

For experimental acquisitions and real-time tests, the different scan sequences were implemented on the ultrasound advanced open platform (ULA-OP 256). It is a complete ultrasound system for research & development; it has 256 independent channels in both transmission and reception and offers full access to the signal data collected at each step of the processing chain. The system consists of eight front-end (FE) boards linked to the master control (MC) board through SerialRapidIO (SRIO) links. Each FE board contains the electronics for: analog conditioning, 32-channel beamforming, and demodulation. The baseband partially-beamformed signals are sent to the MC board, that performs the final beamforming stage, and communicates with the host computer. The latter runs custom real-time software for a last processing stage and visualization.

To increase the number of active channels, multiple ULA-OP 256 systems can be linked together by sharing the same system clock and the same pulse repetition signal. For the purpose of this work, the two ULA-OP 256 systems available at Department of Bioengineering, Imperial College London, were synchronized and connected to the two 256-element sparse arrays.

It is worth highlighting that, when implementing computationally intensive methods in real-time, some of the system specifications could limit the achievable performance. Relevant for this work are:
1. The beamformer maximum data-rate (BBF), expressed as the number of beamformed points per second, BBF=500 MSPS (Mega Samples Per Second);
2. The maximum total transfer-rate between the FE boards and the MC board (BMC), expressed as Gigabytes (10$^9$

bytes) per second, BMC=2.5 GB/s.
When making calculations on this latter parameter, one should consider that each baseband point coming from a FE board has a size of 8 bytes.

Experimental acquisitions and real-time tests were performed by scanning two phantoms. The first one is a wire-target phantom (Model 055A, CIRS Inc., Norfolk, VA); it is manufactured from the water-based polymer developed by CIRS called Zerdine®. The wire-targets on the vertical axis are placed with step-distance of 1 cm and were scanned to assess PSFs. The second phantom was a thick-walled univentricular phantom [44], available at KU Leuven. Such a unique phantom mimics mechanical and acoustic properties of the left ventricle. It was exploited to assess the image contrast performance.

*E. Performance metrics*

*1) Image quality metrics*

Image quality metrics was assessed on both simulations and experiments by processing the quadrature demodulated baseband data (IQ). Specifically, the contrast ratio (CR) was defined as follows:

$$CR = \frac{\int_{C_{ROI}} dS}{\int_{S_{ROI}} dS} \cdot \frac{\int_{S_{ROI}} |IQ(S)|^2\, dS}{\int_{C_{ROI}} |IQ(S)|^2\, dS} \qquad (10)$$

Where the signal region ($S_{ROI}$) and the anechoic region ($C_{ROI}$) were defined as shown in Fig. 5. For experiments only, the signal-to-noise ratio (SNR) was defined as follows:

$$SNR = \frac{\int_{S_{ROI}} |IQ(S)|^2\, dS}{\int_{S_{ROI}} |IQ_N(S)|^2\, dS} \qquad (11)$$

where $IQ_N$ are the quadrature demodulated baseband data with noise only, i.e. obtained with disconnected probe.

The depth dependent lateral resolution was estimated as the full width at half maximum (FWHM) of the point spread functions of point/wire scatterers placed at different depths.

It is worth highlighting that, for experiments, the pre-beamforming signals needed to reconstruct 15 sets of tri-plane images were acquired and post-processed (filtered, beamformed, and demodulated) following the same processing chain of the simulated data. Moreover, CR, SNR, and FWHM were computed as the average values obtained on the 15 sets to limit the impact of electronic noise.
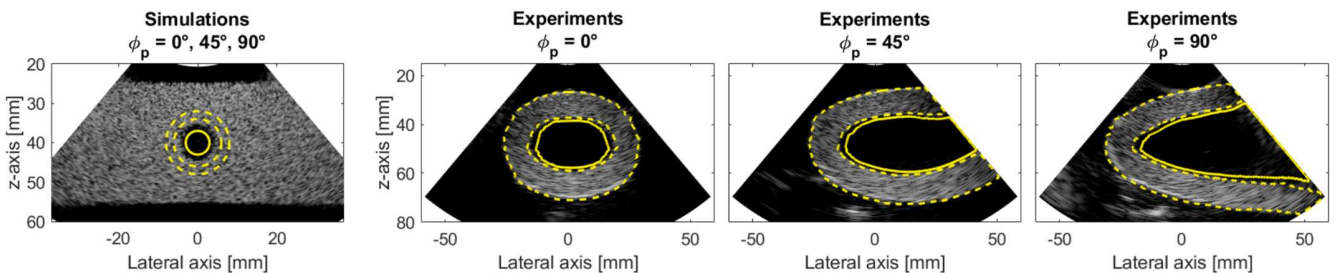


Fig. 5 Selected regions of interest for image quality assessment: the signal region ($S_{ROI}$) is sorrounded between dashed lines, while the anechoic region ($C_{ROI}$) is between solid lines. In simulation, given the symmetry of the phantom, the two regions were the same for the image obtained with different rotational angles.

## 2) Real-time speed performance metrics

The computing capability of the system achieved in real-time was evaluated in terms of maximum frame rate during continuous real-time B-mode imaging ($FR_{Max}$) and maximum pulse repetition frequency ($PRF_{Max}$). The limits on the speed performance were thus motivated by comparing the requirements with the system specifications related to BBF and BMC (refer to section II.D.4), considering the use of all the 8 FE boards.

## III. RESULTS

### A. Image quality metrics

#### 1) Simulations

TABLE I shows CR values obtained in simulations; values are expressed in dB and normalized to the SLT scan sequence. Reading the table from the leftmost column to the rightmost column, the CR decreases on average of about 4.3, 10.7, 11.8dB for MLT, SPT, and MPT respectively. Concerning the probe configurations, PA+PB performed the best and was thus used as reference; mixed configurations, i.e. txPArxPB and txPBrxPA, worsen CR by about 4dB; single array

configurations, i.e. PA and PB, reduce CR by about -6.6dB with respect to PA+PB.

TABLE II shows the relative differences in lateral resolution, averaged for the 4 simulated point scatterers, and normalized to the best performing scan sequence, i.e. MLT. Clearly, the table can be split in two parts: the first, including SLT and MLT having a similar resolution (differences lower than 2.2%); the second part, including SPT and MPT, showing a 50% worse resolution. Concerning the probe configurations, the reference is PB, producing the best lateral resolution; however, overall, the different configurations perform similarly, with a slightly better resolution for PB and txPArxPB.

#### 2) Experiments

TABLE III shows the CR values obtained for the univentricular phantom experiments, expressed in dB and normalized to SLT scan sequence. Reading the table from SLT column to MPT column, the CR decreases on average by about 3.7, 10.0, 11.9dB for MLT, SPT, and MPT, respectively. Concerning the probe configurations, the reference is PA+PB that performed the best; mixed configurations worsen CR of about 1.7dB; single array

TABLE I
SIMULATION RESULTS: CONTRAST RATIO (CR)

| [dB] | SLT | MLT | SPT | MPT |
|---|---|---|---|---|
| PA | 0 (-5.9) | -4.1 | -8.4 | -9.9 |
| PB | 0 (-7.3) | -3.3 | -9.8 | -10.8 |
| txPArxPB | 0 (-3.9) | -5.2 | -12.7 | -12.7 |
| txPBrxPA | 0 (-4.0) | -5.6 | -11.0 | -11.8 |
| PA+PB | 0 (0.0) | -3.3 | -11.5 | -13.9 |

For each probe configuration, dB values are normalized to SLT mode. Values between brackets are normalized to PA+PB configuration, which achieved the best performance (25.6dB).

TABLE II
SIMULATION RESULTS: LATERAL RESOLUTION (FWHM) DIFFERENCES

| [%] | SLT | MLT | SPT | MPT |
|---|---|---|---|---|
| PA | +2.2 | 0 (+0.8) | +54 | +53 |
| PB | +0.8 | 0 (0.0) | +48 | +46 |
| txPArxPB | +1.9 | 0 (+0.3) | +49 | +47 |
| txPBrxPA | +1.1 | 0 (+0.5) | +53 | +51 |
| PA+PB | +1.6 | 0 (0.0) | +50 | +50 |

For each probe configuration, values are expressed in percentage with respect to MLT mode. Values between brackets show percentage values with respect to PB configuration, which achieved the best performance (e.g. 1.9 mm at a depth of 40-mm).

TABLE III
EXPERIMENTAL RESULTS: CONTRAST RATIO (CR)

| [dB] | SLT | MLT | SPT | MPT |
|---|---|---|---|---|
| PA | 0 (-3.2) | -3.1 | -10.0 | -11.4 |
| PB | 0 (-2.8) | -3.5 | -9.0 | -11.3 |
| txPArxPB | 0 (-1.7) | -4.0 | -10.1 | -12.3 |
| txPBrxPA | 0 (-1.7) | -4.5 | -11.3 | -13.3 |
| PA+PB | 0 (0.0) | -3.6 | -9.6 | -11.0 |

For each probe configuration, dB values are normalized to SLT mode. Values between brackets are normalized to PA+PB configuration, which achieved the best performance (27.8dB).

TABLE IV
EXPERIMENTAL RESULTS: LATERAL RESOLUTION (FWHM) DIFFERENCES

| [%] | SLT | MLT | SPT | MPT |
|---|---|---|---|---|
| PA | +4.3 | 0 (+3.7) | +50 | +43 |
| PB | +2.7 | 0 (+0.0) | +50 | +46 |
| txPArxPB | +2.1 | 0 (+2.7) | +48 | +45 |
| txPBrxPA | +2.7 | 0 (+1.8) | +52 | +47 |
| PA+PB | 0.0 | 0 (+2.7) | +42 | +39 |

For each probe configuration, values are expressed in percentage with respect to MLT mode. Values between brackets show percentage values with respect to PB configuration, which achieved the best performance (e.g. 1.8 mm at a depth of 40-mm).

TABLE V
EXPERIMENTAL RESULTS: SIGNAL-TO-NOISE RATIO (SNR)

| | SLT | MLT | SPT | MPT |
|---|---|---|---|---|
| PA | -8.0 | -9.2 | -8.7 | -8.6 |
| PB | -7.2 | -8.4 | -8.0 | -8.1 |
| txPArxPB | -7.5 | -8.8 | -8.3 | -8.2 |
| txPBrxPA | -8.2 | -9.5 | -8.9 | -9.1 |
| PA+PB | 0 (0.0) | 0 (-8.7) | 0 (-9.7) | 0 (-16.7) |

For each imaging mode, dB values are normalized to PA+PB probe configuration. Values between brackets are normalized to SLT mode, which achieved the best performance (39.6dB).

TABLE VI
MEASURED SPEED PERFORMANCE

| | SLT | MLT | SPT | MPT |
|---|---|---|---|---|
| $PRF_U$ [Hz] | 11000 | 11000 | 11000 | 11000 |
| $PRF_{Max}$ [Hz] | 11000 | 11000 | 750 | 250 |
| BBF [MSPS] | 22 | 67 | 152 | 152 |
| BMC [GB/s] | 0.36 | 1.08 | 2.46 | 2.46 |
| $FR_{Max}$ [Hz] | 37 | 110 | 250 | 250 |

The bottlenecks are highlighted in yellow.
The bandwidth limits are: BBF<500 MSPS and BMC<2.50 GB/s.
The maximum depth of interest was set to 70 mm.

configurations reduced CR to about -3.0dB with respect to PA+PB.

TABLE IV shows the relative differences in lateral resolution, averaged for 4 wires (depth: ~30, 40, 50, 60 mm) in the wire-target phantom CIRS 055A, and normalized to the best performing scan sequence, i.e. MLT. SLT and MLT have similar resolution (differences lower than 4.3%); while SPT and MPT, show a worse resolution 48% and 44% respectively. Concerning the probe configurations, the reference is PB, producing the best lateral resolution; however, overall, the different configurations perform similarly, showing resolution increases lower than 3.7%.

TABLE V shows the experimental SNR values obtained for the univentricular phantom experiments, expressed in dB and normalized to PA+PB probe configuration, i.e. the probe with 512 elements that provides the highest SNR values. On average, all probe configurations showed an 8.4dB reduction in SNR. Moreover, also the scan sequence impacted the SNR values; comparing to SLT, i.e. the sequence yielding the best SNR value, a reduction of SNR of 8.7, 9.7, and 16.7dB was shown with MLT, SPT and MPT, respectively.

Fig. 6 shows a comparison among the images obtained with different scan sequences. In particular, focusing on the region centered at $(x, z) = (40, 55)$ mm, the intensity of the artifacts increases in agreement to the reduction of CR shown in TABLE III: the best performing mode is SLT, while the worst is MPT. Specifically, the latter also shows a high intensity stripe, centered at x=0 mm, due to the superposition of the 3 diverging waves generating a higher intensity in transmission, which might be compensated by exploiting simulations similar to those shown in Fig. 3, but obtained for all depths of interest. Moreover, Fig. 6 confirms the worse resolution of the imaging modes based on the transmission of diverging waves (SPT, MPT); clearly, the speckle of SPT and MPT is less sharp compared to SLT and MLT.

## B. Real-time speed performance metrics

TABLE VI shows the measured speed performance of the system for the different imaging modes. Given that all probe configurations use the maximum number of channels per system (256), the speed performance does not depend on the probe configuration. It is worth highlighting that for PA+PB the two systems were transmitting simultaneously, but two partially beamformed images were reconstructed in real-time, one for each system; the final image, i.e. the sum of the two above, could not be seen in real-time and was computed offline.

Speed performance tests were made for a depth range of 10-70 mm; the radiofrequency beamforming was set for an output sampling frequency of 26 MHz. This means that the maximum unambiguous PRF ($PRF_U$) is 11000 Hz and that the number of beamformed depths is 2048.

According to TABLE VI, SLT and MLT modes were only limited by the maximum depth that limited the PRF, while BBF and BMC were well below their maximum sustainable transfer rates. SLT and MLT respectively achieved a frame rate of 37 and 110 Hz. On the other hand, SPT and MPT were limited by BMC: in this work, for a full set of tri-plane frame, 300 lines ($nL \times nP = 100 \times 3$, i.e. 100 lines per imaging plane) were reconstructed, and for each line 512 baseband samples were transferred, corresponding to a total of 153600 32-bit complex samples per frame for each FE board. Thus, the transfer bandwidth limit of 2.50 GB/s was reached for both SPT and MPT when the frame rate was 250 Hz.

Fig. 7 shows a screenshot of the ULA-OP 256 real-time interface during experimental tri-plane imaging of the
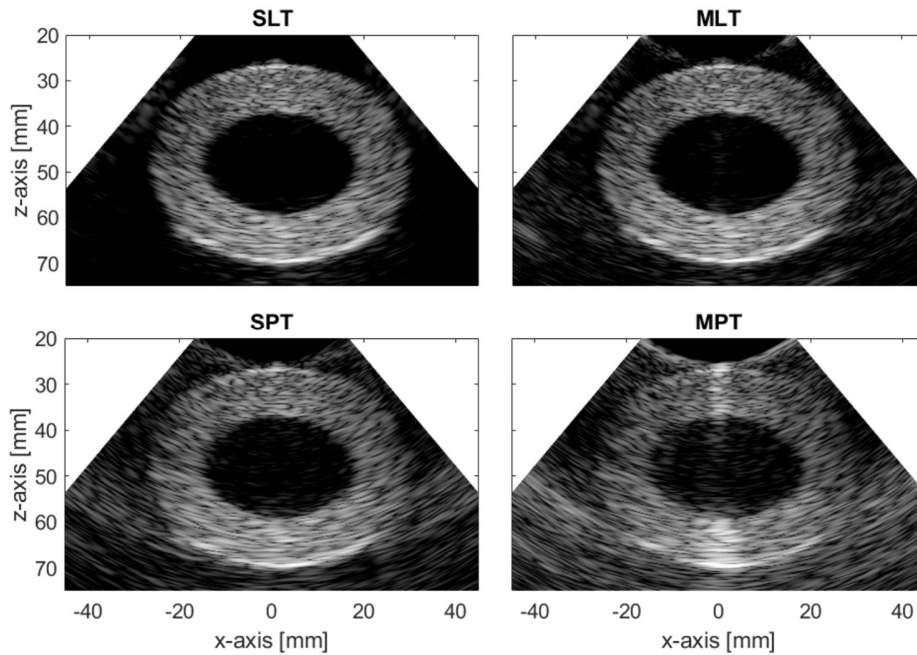


Fig. 6 Qualitative comparison among imaging modes. The panels show the B-mode experimental images of the univentricular phantom; the plane with rotational angle equal to 0° was selected and the dynamic range was set to 45dB.
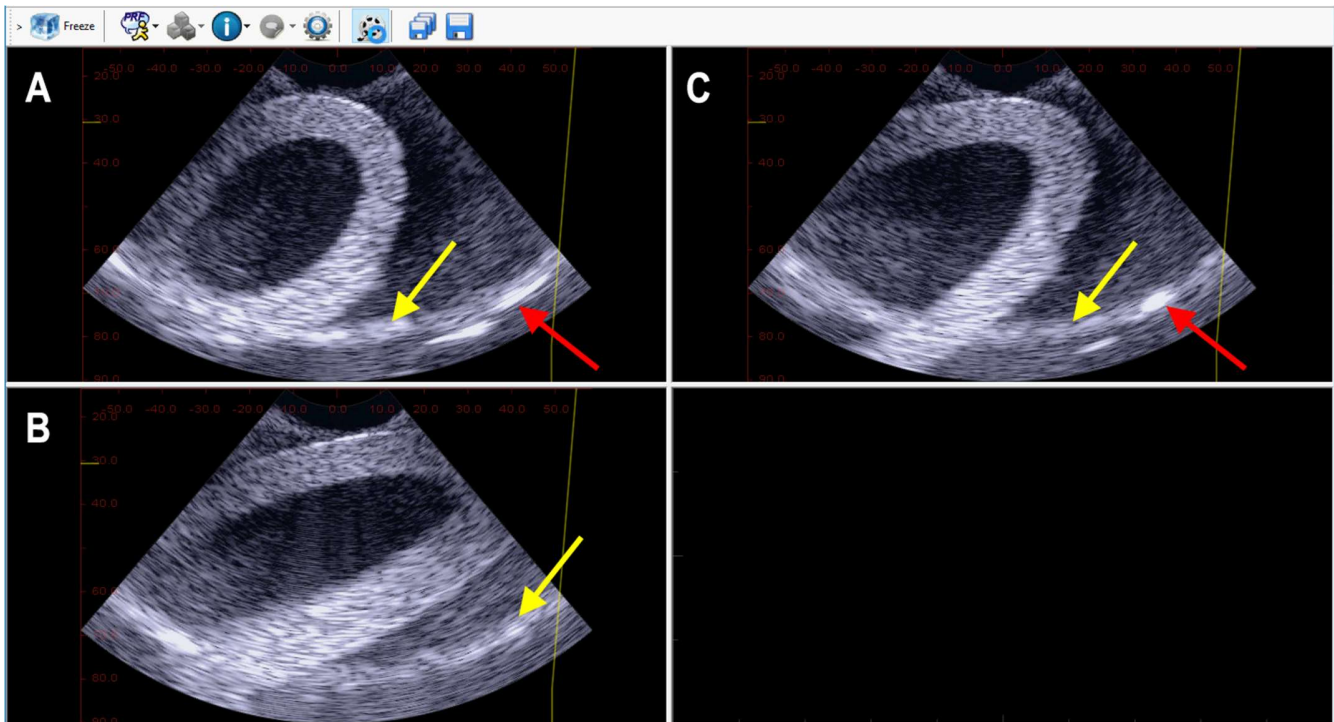
Fig. 7 ULA-OP 256 real-time interface frame (extracted from the accompayning movie clip 🎦) during MLT tri-plane imaging of the univentricular phantom; the probe was set in configuration PA. The different panels show the B-mode images reconstructed at different rotation angles: 0° (A), 45° (B), and 90° (C). Red arrows point to the bottom of the tank; yellow arraows point the artifacts due to the bottom of the tank.

univentricular phantom. The 3 panels display the B-mode images obtained for different rotational angles: 0° (A), 45° (B), and 90° (C). In this example, the selected array was PA, while the imaging mode was MLT. The accompanying movie clip 🎦, from which Fig. 7 was extracted, proves the continuous real-time capability of the system.

## IV. DISCUSSION

In this paper, we have presented a study of high frame rate tri-plane imaging for echocardiography using spiral arrays. The method was first simulated, then experimentally validated, and finally implemented on the ULA-OP 256 system for real-time operation. Five different probe configurations together with four different scan sequences were tested. Qualitative and quantitative results have been shown together with a movie clip of the real-time interface of the ULA-OP 256 system captured during phantom experiments.

Image quality was assessed on numerical and experimental phantoms in terms of CR, lateral resolution, and SNR. Overall, simulation and experimental results were in good agreement and showed very similar trends. CR, as expected, depends on the scan sequence, but in particular, as shown in Fig. 3 and the related accompanying movie clip, it depends on the acoustic energy spread over the region of interest. Indeed, as summarized in TABLE I and TABLE III, higher CR values are obtained for SLT mode that focuses the energy only along one direction per transmission event, thus artifacts are mainly due to side- and grating-lobes. MLT, even if it is still a

focused mode, focuses simultaneously along 3 directions, one per imaging plane, thus contrast is mainly affected by beam cross-talk artifacts. The worst contrast is obtained with the transmission of diverging waves since the energy is spread on a broad region of interest: one plane for SPT and three planes for MPT. Qualitatively, it was also confirmed in Fig. 6 that highlights how the higher level of artifacts is linked to the imaging mode. Specifically, the contrast on MPT images is also affected by the brightness irregularity close to the central lines; here, the images is brighter due to the superposition of the three diverging waves generating higher peak pressures, as shown in Fig. 3.

Even if at a minor extent, also the array configuration impacts the CR. The best CR is always obtained with the configuration PA+PB, that, among the others, has the densest aperture, thus reducing grating-lobes and consequently artifacts. Mixed configurations (txPArxPB and txPBrxPA) perform better than single array configurations (PA and PB); indeed, the direction of the maxima of side-lobes and grating-lobes are most likely different between the transmission and the reception beams, due to the different distribution of the elements on the transmitting and receiving arrays.

In terms of lateral resolution (TABLE II and TABLE IV), focused modes (SLT and MLT) perform similarly, even though an unexpected slight resolution improvement is observed for MLT. Although such improvement is quite limited, it could be worth performing further studies to gain a better insight into it. On the other hand, lateral resolution is degraded significantly (roughly +50%) for SPT and MPT modes due to the lack of focusing in transmission while using

diverging waves. It is worth noting that the effect of different probe configurations on the resolution is negligible as their equivalent apertures are similar; approximating them as twice the average distance between the position of the active elements and the center of the probe, they were 5.4, 5.7, 5,6 mm for PA, PB, and PA+PB, respectively. The slightly wider aperture of PB also explains the marginally better resolution obtained with PB compared to the other configurations.

The SNR (TABLE V) depends on both probe configuration and imaging mode. The impact of the former, mainly depends on the number of active elements; hence, the array PA+PB, having 512 transmitting and receiving elements, produces a 8.4dB higher SNR than all the other configurations having 256 elements. Such higher value is in-line with the expected one; indeed, doubling the elements in both transmission and in reception should give 9dB higher SNR values [45]. Also, the imaging mode impacts the SNR to the same extent as the energy is focused in transmission or not. For example, SLT achieves a higher SNR (+8.7dB) compared to SPT. Furthermore, MLT and MPT achieve lower SNR values compared to SLT and SPT: −8.7dB and −7dB respectively. The reason why this drop happens is that, for MLT and MPT, the average level of energy transmitted by the different elements is lower. Indeed, due to the need of keeping peak voltages below the maximum allowed to avoid the depolarization of the transducers, 3-fold lower transmission amplitudes must be used for all elements.

The design of the different layouts of the probe was based on spiral arrays since they are defined by a deterministic equation and guarantee uniform performance over a wide range of steering angles. Other optimized sparse configurations could have been considered, as proposed in the literature [32], [46], [47], but optimizing the layout of a sparse array for the transmission of both focused and diverging waves, while simultaneously scanning planes along different rotational angles, would have been a cumbersome process that might not have led to significant benefits, as already shown in [35]. Anyway, the design of the different arrays was based on a thorough simulation study addressed to compare the performance of the different layouts. The results of the study were not shown in this paper for the sake of synthesis and clarity, nevertheless the most significant outcomes can be summarized as:

1. Forcing the spiral configuration on a gridded layout, for the chosen density tapering (Tukey), had a negligible impact on the imaging performance of PA compared to SA. Also, PB performed similarly to SB even if it presented slightly higher grating lobes (+0.9dB in average) and better resolution (−4.5% in average).

2. The reduction of the number of elements, as expected, has a significant impact on the performance. Specifically, on average, the sparse array configurations, with respect to the 1024-element array probe, achieved: worse lateral resolution (+18%), due to a narrower effective aperture; worse contrast (−2dB for PA+PB), due to the sparsity of the element. Also, for 256-element layouts the SNR is expected to drop

down by 18dB, while for PA+PB the reduction is expected to be 9dB [45].

In general, limited CR and resolution can be improved by employing advanced imaging techniques such as: image coherent compounding, which, even if it limits the frame rate, has already been shown to be effective for cardiac applications based on the transmission of diverging waves [20], [21], [48]; coherence based beamforming methods in reception, enabling both improved spatial resolution and contrast [49]–[52]; adaptive and minimum variance beamformers for artifacts rejection [53]–[56]; the transmission of coded signals for the suppression of cross-talk artifacts in multiline transmission imaging [57], [58]. Also, we showed that mixed array configurations, compared to single array configurations, have a positive impact on CR; nevertheless, a further improvement could be achieved by optimizing the selection of active elements to be assigned to the transmitting and to the receiving arrays [46], [47], [59]. It is worth emphasizing that mixed configurations also have a secondary advantage: they allow keeping the transmission and reception circuits separate. It may further simplify the front-end electronics, but it would double both the number of coaxial cables inside the probe cable and the number of connectors.

Special reference also needs to be made to second harmonic imaging: even if it is typically used in echocardiography to improve image quality [60], [61], it is not yet a feasible option for our purposes. Indeed, the main weakness of our approach (and in general of sparse arrays) is the reduced sensitivity due to the limited size of active elements and their sparse distribution over the active aperture. It is thus difficult to emit high pressures to induce non-linear propagation and to detect very weak signals, as needed in second harmonic imaging.

The lower SNR due to limited sensitivity was, in our case, further worsened by the lack of in-probe signal amplifiers. This increased the susceptibility to electronic noise in reception, thus impacting on the maximum imaging depth. The latter one, possibly, could be increased by implementing coded imaging techniques that implement the transmission of long coded signals and the reception into matched filters [62]–[65]. Employing techniques to compensate the limited SNR would also enable Doppler imaging, either pulsed-wave Doppler or color flow imaging. Indeed, some of the authors have already experimentally assessed that the use of a sparse array, rather than a dense one, do not appreciably impact on the Doppler spectrum shape as well as on its mean frequency, but only on the SNR [66].

The proposed imaging methods were evaluated according to their real-time performance achieved with the ULA-OP 256 system. The limits of these imaging methods, related to maximum depth of interest, beamforming processing speed (BBF), and data transfer rate to the MC board (BMC), were disclosed by showing their performance in terms of $FR_{Max}$ and $PRF_{Max}$. TABLE VI highlights that SLT and MLT modes achieved the maximum physical limit on the PRF for the given depth of interest, here it was set to 70 mm that was arbitrarily chosen as the maximum achievable penetration depth due to the SNR limitation. $FR_{Max}$ for SLT and MLT was 37 Hz and

100 Hz, respectively. On the other hand, SPT and MPT modes were limited by BMC, thus $FR_{Max}$ was 250 Hz for both the modes, i.e. 2.3 times higher than MLT.

Nevertheless, in a more realistic scenario, for cardiac applications the maximum depth of interest should be increased up to 150 mm (see TABLE VII), corresponding to a non-ambiguous PRF of 5000 Hz ($PRF_U$=5000 Hz). Again, $PRF_{Max}$ was the limitation for SLT and MLT, further reducing $FR_{Max}$ to 17 Hz and 50 Hz, respectively. Also, BMC still was the bottleneck for SPT and MPT. Even if and increased number of beamformed samples pushed up the computational load on the beamformers (BBF up to 365 MSPS in TABLE VII), BBF was well below the maximum sustainable, hence $FR_{Max}$ remained limited to 250 Hz by BMC, that was 5 times higher than MLT. Further speculating with those figures, we estimated that the limits on both BMC (2.50 GB/s) and BBF (500 MSPS) would be simultaneously reached when producing frames with 390 depths per line (instead of 512) and with a PRF of 1000 Hz and 333 Hz for SPT and MPT, respectively; thus, the resulting $FR_{Max}$ for a maximum depth of interest of 150 mm would be 333 Hz.

It may be observed that $FR_{Max}$ of SPT and MPT is always the same; it is worth highlighting that it will remain the same, even in ideal absence of data rate limits, until $FR_{Max}$ of SPT will be only limited by the PRF, e.g. until $FR_{Max}$ will be equal to 5000/3 Hz for a depth of interest of 150 mm. For real-time applications, it is not worth implementing those imaging modes that theoretically allow achieving very high frame rates, as long as the system architecture, the electronics, or the computational load do not allow achieving the non-ambiguous PRF for the imaging depth of interest. Instead, it would be preferable implementing smarter imaging modes that could achieve, in real-time, the same $FR_{Max}$ but with an improved quality of images. For example, since the current architecture of the ULA-OP 256 system allows reconstructing up to 32 lines per transmission event, when being limited by $PRF_{Max}$ [43] in real-time cardiac applications, SPT is too much demanding (100 lines per transmission event) and a different transmission scheme should be implemented. An option could be the transmission of diverging waves having narrower aperture angles to scan each plane in several (e.g. 3) consecutive transmissions [67], [68]; this would reduce both the number of lines to be reconstructed for each transmission event and the energy spread over the region of interest with benefits in terms of CR and SNR without impacting on the achievable FR in real-time.

In general, continuous real-time HFR imaging is beneficial when subsequent processing is applied to produce additional information in real-time, e.g. tissue-motion [43] or color flow imaging [69]. For example, through the implementation of a speckle tracking technique, the frame rate achieved in this work with SPT and MPT (250 Hz) might enable real-time functional analysis of all left ventricular segments of the heart. Nevertheless, in some cases, a discontinuous real-time display and a delayed continuous presentation of results could be sufficient, thus relaxing the requirements in terms of computational power while making the memory requirements

### TABLE VII
MEASURED SPEED PERFORMANCE
FOR A MAXIMUM DEPTH OF INTEREST OF 150 MM

|  | SLT | MLT | SPT | MPT |
|---|---|---|---|---|
| **$PRF_U$ [Hz]** | 5000 | 5000 | 5000 | 5000 |
| **$PRF_{Max}$ [Hz]** | 5000 | 5000 | 750 | 250 |
| **BBF [MSPS]** | 24 | 73 | 365 | 365 |
| **BMC [GB/s]** | 0.16 | 0.49 | 2.46 | 2.46 |
| **$FR_{Max}$ [Hz]** | 17 | 50 | 250 | 250 |

The bottlenecks are highlighted in yellow.
The bandwidth limits are: BBF<500 MSPS and BMC<2.50 GB/s.

more demanding. To this end, typically, few-second-long acquisitions are performed at the maximum PRF, calmly post-processed on the system, and then results are shown after few seconds. This option, available on the ULA-OP 256 system as well as in other research scanners, would allow increasing the frame rate by exploiting SPT and MPT or full 3D HFR by the use of fully diverging waves [10]–[12].

To summarize, low-element count scanners (less complex and less expensive) are suitable for high frame rate tri-plane echocardiography, however the simpler system design and improved temporal resolution come at the expense of image quality, in terms of SNR, spatial resolution, and CR. The best performance was indeed obtained with the dense configuration exploiting more elements, i.e. PA+PB. MLT can be exploited to achieve in tri-plane imaging the same temporal resolution currently used in clinical 2D echocardiography. Moreover, being realistic, reconstructing hundreds of lines in parallel for each transmission event is still not an option in real-time, even with a different system architecture and a different processing pipeline, e.g. by direct sampling IQ beamforming [70]. Therefore, even if MPT could achieve, in post-processing, frame rates as high as those obtained with fully diverging waves, it is not yet a feasible option in continuous real-time imaging since it allows achieving the same $FR_{Max}$ of SPT but producing images with worse CR and SNR values.

Finally, for a qualitative comparison of the currently achievable imaging performance, preliminary in-vivo acquisitions were performed by an expert sonographer on a 35-year-old healthy volunteer. The focal depth was set to 80 mm, the maximum depth of interest to 150 mm, and the 3 rotational angles to 0°, 60° and 120°. The ULA-OP 256 real-time interface was captured while simultaneously scanning the 4-, 3-, and 2-chamber views either with SLT 🎥, MLT 🎥, or SPT 🎥. The movie clips, as deeply discussed above, confirm the limited resolution and contrast obtained with SPT and a low SNR with all the scan sequences. Nevertheless, despite all these limitations and the fact that no image filter was used (i.e. these are raw images), the main cardiac views are recognizable. Of course, improvements are needed to make this approach useful in clinical practice.

### V. CONCLUSION & PERSPECTIVE

We have presented an extensive study for the development of an advanced ultrasound system for real-time high frame rate tri-plane echocardiography. We showed that, despite an unavoidable loss in image quality and sensitivity, tri-plane

imaging using MLT and planar diverging waves with sparse arrays is feasible in real-time. MLT allows achieving, in tri-plane imaging, the same temporal resolution currently used in clinical 2D echocardiography, while the transmission of planar diverging waves boosts the frame rate up to 250 Hz and may enable real-time functional analysis of the heart using a system with low element and channel count.

Future developments, required before a clinical applicability of the systems, should include:
- In-probe signal amplifiers and coded imaging techniques to improve SNR and penetration depth;
- The implementation of smarter imaging modes to improve both contrast and resolution in diverging wave imaging;
- The ability to change, on the fly, the rotational angles of the 3 imaging planes to adapt them to the specific anatomy of the subject; the best would be an automatic selection of the views, e.g. by machine learning [71].

## REFERENCES

[1] E. Wilkins *et al.*, "European Cardiovascular Disease Statistics 2017," *Eur. Heart Netw.*, Feb. 2017.

[2] E. J. Benjamin *et al.*, "Heart Disease and Stroke Statistics—2018 Update: A Report From the American Heart Association," *Circulation*, vol. 137, no. 2, pp. e67–e492, Jan. 2018.

[3] M. M. Redfield, S. J. Jacobsen, J. John C. Burnett, D. W. Mahoney, K. R. Bailey, and R. J. Rodeheffer, "Burden of Systolic and Diastolic Ventricular Dysfunction in the Community: Appreciating the Scope of the Heart Failure Epidemic," *JAMA*, vol. 289, no. 2, pp. 194–202, Jan. 2003.

[4] E. D. Light, S. F. Idriss, P. D. Wolf, and S. W. Smith, "Real-time three-dimensional intracardiac echocardiography," *Ultrasound Med. Biol.*, vol. 27, no. 9, pp. 1177–1183, Sep. 2001.

[5] R. M. Lang, V. Mor-Avi, L. Sugeng, P. S. Nieman, and D. J. Sahn, "Three-Dimensional Echocardiography: The Benefits of the Additional Dimension," *J. Am. Coll. Cardiol.*, vol. 48, no. 10, pp. 2053–2069, Nov. 2006.

[6] S. Yagel, S. M. Cohen, I. Shapiro, and D. V. Valsky, "3D and 4D ultrasound in fetal cardiac scanning: a new look at the fetal heart," *Ultrasound Obstet. Gynecol.*, vol. 29, no. 1, pp. 81–95, Jan. 2007.

[7] Mor-Avi Victor, Sugeng Lissa, and Lang Roberto M., "Real-Time 3-Dimensional Echocardiography," *Circulation*, vol. 119, no. 2, pp. 314–329, Jan. 2009.

[8] A. M. Johri, J. J. Passeri, and M. H. Picard, "Three dimensional echocardiography: approaches and clinical utility," *Heart*, vol. 96, no. 5, pp. 390–397, Mar. 2010.

[9] D. P. Shattuck, M. D. Weinshenker, S. W. Smith, and O. T. von Ramm, "Explososcan: A parallel processing technique for high speed ultrasound imaging with linear phased arrays," *J. Acoust. Soc. Am.*, vol. 75, no. 4, pp. 1273–1282, 1984.

[10] J. Provost *et al.*, "3D ultrafast ultrasound imaging in vivo," *Phys. Med. Biol.*, vol. 59, no. 19, pp. L1–L13, Oct. 2014.

[11] L. Petrusca *et al.*, "Fast Volumetric Ultrasound B-Mode and Doppler Imaging with a New High-Channels Density Platform for Advanced 4D Cardiac Imaging/Therapy," *Appl. Sci.*, vol. 8, no. 2, p. 200, Feb. 2018.

[12] C. Papadacci *et al.*, "4D simultaneous tissue and blood flow Doppler imaging: revisiting cardiac Doppler index with single heart beat 4D ultrafast echocardiography," *Phys. Med. Biol.*, vol. 64, no. 8, p. 085013, Apr. 2019.

[13] L. Sugeng *et al.*, "Biplane stress echocardiography using a prototype matrix-array transducer," *J. Am. Soc. Echocardiogr.*, vol. 16, no. 9, pp. 937–941, Sep. 2003.

[14] A. Franke, "Real-time Three-Dimensional Echocardiography in Stress Testing: Bi- and Triplane Imaging for Enhanced Image Acquisition," *Cardiol. Clin.*, vol. 25, no. 2, pp. 261–265, May 2007.

[15] E. Eroglu *et al.*, "Comparison of real-time tri-plane and conventional 2D dobutamine stress echocardiography for the assessment of coronary artery disease," *Eur. Heart J.*, vol. 27, no. 14, pp. 1719–1724, Jul. 2006.

[16] N. R. V. de Veire *et al.*, "Triplane tissue Doppler imaging: a novel three-dimensional imaging modality that predicts reverse left ventricular remodelling after cardiac resynchronisation therapy," *Heart*, vol. 94, no. 3, pp. e9–e9, Mar. 2008.

[17] K. Shahgaldi, P. Gudmundsson, A. Manouras, L.-Å. Brodin, and R. Winter, "Visually estimated ejection fraction by two dimensional and triplane echocardiography is closely correlated with quantitative ejection fraction by real-time three dimensional echocardiography," *Cardiovasc. Ultrasound*, vol. 7, no. 1, p. 41, Aug. 2009.

[18] J. Cheng and J.-Y. Lu, "Extended high-frame rate imaging method with limited-diffraction beams," *IEEE Trans. Ultrason. Ferroelectr. Freq. Control*, vol. 53, no. 5, pp. 880–899, May 2006.

[19] H. Hasegawa and H. Kanai, "High-frame-rate echocardiography using diverging transmit beams and parallel receive beamforming," *J. Med. Ultrason.*, vol. 38, no. 3, pp. 129–140, May 2011.

[20] C. Papadacci, M. Pernot, M. Couade, M. Fink, and M. Tanter, "High-contrast ultrafast imaging of the heart," *IEEE Trans. Ultrason. Ferroelectr. Freq. Control*, vol. 61, no. 2, pp. 288–301, Feb. 2014.

[21] J. Poree, D. Posada, A. Hodzic, F. Tournoux, G. Cloutier, and D. Garcia, "High-Frame-Rate Echocardiography Using Coherent Compounding With Doppler-Based Motion-Compensation," *IEEE Trans. Med. Imaging*, vol. 35, no. 7, pp. 1647–1657, Jul. 2016.

[22] A. Ortega *et al.*, "A Comparison of the Performance of Different Multiline Transmit Setups for Fast Volumetric Cardiac Ultrasound," *IEEE Trans. Ultrason. Ferroelectr. Freq. Control*, vol. 63, no. 12, pp. 2082–2091, Dec. 2016.

[23] S. Fadnes, M. S. Wigen, S. A. Nyrnes, and L. Lovstakken, "In Vivo Intracardiac Vector Flow Imaging Using Phased Array Transducers for Pediatric Cardiology," *IEEE Trans. Ultrason. Ferroelectr. Freq. Control*, vol. 64, no. 9, pp. 1318–1326, Sep. 2017.

[24] P. Santos *et al.*, "Natural shear wave imaging in the human heart: normal values, feasibility and reproducibility," *IEEE Trans. Ultrason. Ferroelectr. Freq. Control*, vol. 66, no. 3, pp. 442–452, Mar. 2019.

[25] L. Demi, "Practical Guide to Ultrasound Beam Forming: Beam Pattern and Image Reconstruction Analysis," *Appl. Sci.*, vol. 8, no. 9, p. 1544, Sep. 2018.

[26] B. Savord and R. Solomon, "Fully sampled matrix transducer for real time 3D ultrasonic imaging," in *2003 IEEE Ultrasonics Symposium (IUS)*, 2003, vol. 1, pp. 945–953.

[27] J.D. Larson III, "2-d phased array ultrasound imaging system with distributed phasing," Pat. US5229933 A, Jul-1993.

[28] A. Savoia *et al.*, "Crisscross 2D cMUT Array: Beamforming Strategy and Synthetic 3D Imaging Results," in *2007 IEEE Ultrasonics Symposium Proceedings*, 2007, pp. 1514–1517.

[29] C. H. Seo and J. T. Yen, "A 256 x 256 2-D array transducer with row-column addressing for 3-D rectilinear imaging," *IEEE Trans. Ultrason. Ferroelectr. Freq. Control*, vol. 56, no. 4, pp. 837–847, Apr. 2009.

[30] M. F. Rasmussen, T. L. Christiansen, E. V. Thomsen, and J. A. Jensen, "3-D imaging using row-column-addressed arrays with integrated apodization - part i: apodization design and line element beamforming," *IEEE Trans. Ultrason. Ferroelectr. Freq. Control*, vol. 62, no. 5, pp. 947–958, May 2015.

[31] R. E. Davidsen, J. A. Jensen, and S. W. Smith, "Two-dimensional random arrays for real time volumetric imaging," *Ultrason. Imaging*, vol. 16, no. 3, pp. 143–163, Jul. 1994.

[32] A. Austeng and S. Holm, "Sparse 2-D arrays for 3-D phased array imaging - design methods," *IEEE Trans. Ultrason. Ferroelectr. Freq. Control*, vol. 49, no. 8, pp. 1073–1086, Aug. 2002.

[33] B. Diarra, M. Robini, P. Tortoli, C. Cachard, and H. Liebgott, "Design of Optimal 2-D Nongrid Sparse Arrays for Medical Ultrasound," *IEEE Trans. Biomed. Eng.*, vol. 60, no. 11, pp. 3093–3102, Nov. 2013.

[34] A. Ramalli, E. Boni, A. S. Savoia, and P. Tortoli, "Density-tapered spiral arrays for ultrasound 3-D imaging," *IEEE Trans. Ultrason. Ferroelectr. Freq. Control*, vol. 62, no. 8, pp. 1580–1588, Aug. 2015.

[35] E. Roux, A. Ramalli, P. Tortoli, C. Cachard, M. C. Robini, and H. Liebgott, "2-D Ultrasound Sparse Arrays Multidepth Radiation Optimization Using Simulated Annealing and Spiral-Array Inspired Energy Functions,"

This article has been accepted for publication in a future issue of this journal, but has not been fully edited. Content may change prior to final publication. Citation information: DOI 10.1109/TUFFC.2019.2940289, IEEE Transactions on Ultrasonics, Ferroelectrics, and Frequency Control

12

*IEEE Trans. Ultrason. Ferroelectr. Freq. Control*, vol. 63, no. 12, pp. 2138–2149, Dec. 2016.

[36] J. A. Jensen and N. B. Svendsen, "Calculation of pressure fields from arbitrarily shaped, apodized, and excited ultrasound transducers," *IEEE Trans. Ultrason. Ferroelectr. Freq. Control*, vol. 39, no. 2, pp. 262–267, Mar. 1992.

[37] J. A. Jensen, "FIELD: A Program for Simulating Ultrasound Systems," *Med. Biol. Eng. Comput.*, vol. 34, no. Supplement 1, Part 1, pp. 351–353, 1996.

[38] E. Boni *et al.*, "Architecture of an Ultrasound System for Continuous Real-Time High Frame Rate Imaging," *IEEE Trans. Ultrason. Ferroelectr. Freq. Control*, vol. 64, no. 9, pp. 1276–1284, Sep. 2017.

[39] R. Jasaityte *et al.*, "Comparison of a new methodology for the assessment of 3D myocardial strain from volumetric ultrasound with 2D speckle tracking," *Int. J. Cardiovasc. Imaging*, vol. 28, no. 5, pp. 1049–1060, Jun. 2012.

[40] L. Tong, A. Ramalli, R. Jasaityte, P. Tortoli, and J. D'hooge, "Multi-Transmit Beam Forming for Fast Cardiac Imaging: Experimental Validation and In Vivo Application," *IEEE Trans. Med. Imaging*, vol. 33, no. 6, pp. 1205–1219, Jun. 2014.

[41] Y. Chen, L. Tong, A. Ortega, J. Luo, and J. D'hooge, "Feasibility of Multiplane-Transmit Beamforming for Real-Time Volumetric Cardiac Imaging: A Simulation Study," *IEEE Trans. Ultrason. Ferroelectr. Freq. Control*, vol. 64, no. 4, pp. 648–659, Apr. 2017.

[42] A. Ramalli, P. Santos, P. Tortoli, and J. D'hooge, "Tri-Plane Cardiac Imaging Using Multi-Line Transmission on a Spiral Array: A Feasibility Study," in *2018 IEEE International Ultrasonics Symposium (IUS)*, 2018, pp. 1–4.

[43] A. Ramalli *et al.*, "Real-Time High-Frame-Rate Cardiac B-Mode and Tissue Doppler Imaging Based on Multiline Transmission and Multiline Acquisition," *IEEE Trans. Ultrason. Ferroelectr. Freq. Control*, vol. 65, no. 11, pp. 2030–2041, Nov. 2018.

[44] B. Heyde *et al.*, "Regional cardiac motion and strain estimation in three-dimensional echocardiography: a validation study in thick-walled univentricular phantoms," *IEEE Trans. Ultrason. Ferroelectr. Freq. Control*, vol. 59, no. 4, pp. 668–682, Apr. 2012.

[45] E. Roux, F. Varray, L. Petrusca, C. Cachard, P. Tortoli, and H. Liebgott, "Experimental 3-D Ultrasound Imaging with 2-D Sparse Arrays using Focused and Diverging Waves," *Sci. Rep.*, vol. 8, no. 1, p. 9108, Jun. 2018.

[46] E. Roux, A. Ramalli, H. Liebgott, C. Cachard, M. C. Robini, and P. Tortoli, "Wideband 2-D Array Design Optimization With Fabrication Constraints for 3-D US Imaging," *IEEE Trans. Ultrason. Ferroelectr. Freq. Control*, vol. 64, no. 1, pp. 108–125, Jan. 2017.

[47] A. Trucco, "Thinning and weighting of large planar arrays by simulated annealing," *IEEE Trans. Ultrason. Ferroelectr. Freq. Control*, vol. 46, no. 2, pp. 347–355, Mar. 1999.

[48] J. Grondin, V. Sayseng, and E. E. Konofagou, "Cardiac Strain Imaging With Coherent Compounding of Diverging Waves," *IEEE Trans. Ultrason. Ferroelectr. Freq. Control*, vol. 64, no. 8, pp. 1212–1222, Aug. 2017.

[49] J. Camacho, M. Parrilla, and C. Fritsch, "Phase Coherence Imaging," *IEEE Trans. Ultrason. Ferroelectr. Freq. Control*, vol. 56, no. 5, pp. 958–974, May 2009.

[50] M. A. Lediju, G. E. Trahey, B. C. Byram, and J. J. Dahl, "Short-lag spatial coherence of backscattered echoes: imaging characteristics," *IEEE Trans. Ultrason. Ferroelectr. Freq. Control*, vol. 58, no. 7, pp. 1377–1388, Jul. 2011.

[51] G. Matrone, A. Ramalli, A. S. Savoia, P. Tortoli, and G. Magenes, "High Frame-Rate, High Resolution Ultrasound Imaging With Multi-Line Transmission and Filtered-Delay Multiply And Sum Beamforming," *IEEE Trans. Med. Imaging*, vol. 36, no. 2, pp. 478–486, Feb. 2017.

[52] G. Matrone and A. Ramalli, "Spatial Coherence of Backscattered Signals in Multi-Line Transmit Ultrasound Imaging and Its Effect on Short-Lag Filtered-Delay Multiply and Sum Beamforming," *Appl. Sci.*, vol. 8, no. 4, p. 486, Mar. 2018.

[53] P.-C. Li and M.-L. Li, "Adaptive imaging using the generalized coherence factor," *IEEE Trans. Ultrason. Ferroelectr. Freq. Control*, vol. 50, no. 2, pp. 128–141, Feb. 2003.

[54] Z. Wang, J. Li, and R. Wu, "Time-delay- and time-reversal-based robust capon beamformers for ultrasound imaging," *IEEE Trans. Med. Imaging*, vol. 24, no. 10, pp. 1308–1322, Oct. 2005.

[55] B. M. Asl and A. Mahloojifar, "Eigenspace-based minimum variance beamforming applied to medical ultrasound imaging," *IEEE Trans. Ultrason. Ferroelectr. Freq. Control*, vol. 57, no. 11, pp. 2381–2390, Nov. 2010.

[56] G. Zurakhov *et al.*, "Multiline Transmit Beamforming Combined With Adaptive Apodization," *IEEE Trans. Ultrason. Ferroelectr. Freq. Control*, vol. 65, no. 4, pp. 535–545, Apr. 2018.

[57] L. Demi, A. Ramalli, E. Boni, and J. D'hooge, "Orthogonal Frequency Division Multiplexing Combined with Multi Line Transmission for Ultrafast Ultrasound Imaging: Experimental Findings," in *2018 IEEE International Ultrasonics Symposium (IUS)*, 2018, pp. 1–4.

[58] L. Tong *et al.*, "Coded Excitation for Crosstalk Suppression in Multi-line Transmit Beamforming: Simulation Study and Experimental Validation," *Appl. Sci.*, vol. 9, no. 3, p. 486, Jan. 2019.

[59] C. Sciallero and A. Trucco, "Design of a sparse planar array for optimized 3D medical ultrasound imaging," in *23rd European Signal Processing Conference (EUSIPCO)*, 2015.

[60] F. Prieur, B. Dénarié, A. Austeng, and H. Torp, "Correspondence - Multi-line transmission in medical imaging using the second-harmonic signal," *IEEE Trans. Ultrason. Ferroelectr. Freq. Control*, vol. 60, no. 12, pp. 2682–2692, Dec. 2013.

[61] M. Correia, J. Provost, S. Chatelin, O. Villemain, M. Tanter, and M. Pernot, "Ultrafast Harmonic Coherent Compound (UHCC) Imaging for High Frame Rate Echocardiography and Shear-Wave Elastography," *IEEE Trans. Ultrason. Ferroelectr. Freq. Control*, vol. 63, no. 3, pp. 420–431, Mar. 2016.

[62] T. Misaridis and J. A. Jensen, "Use of modulated excitation signals in medical ultrasound. Part I: basic concepts and expected benefits," *IEEE Trans. Ultrason. Ferroelectr. Freq. Control*, vol. 52, no. 2, pp. 177–191, Feb. 2005.

[63] R. Y. Chiao and Xiaohui Hao, "Coded excitation for diagnostic ultrasound: a system developer's perspective," *IEEE Trans. Ultrason. Ferroelectr. Freq. Control*, vol. 52, no. 2, pp. 160–170, Feb. 2005.

[64] M. Lewandowski and A. Nowicki, "High frequency coded imaging system with RF software signal processing," *IEEE Trans. Ultrason. Ferroelectr. Freq. Control*, vol. 55, no. 8, pp. 1878–1882, 2008.

[65] A. Ramalli, F. Guidi, E. Boni, and P. Tortoli, "A real-time chirp-coded imaging system with tissue attenuation compensation," *Ultrasonics*, vol. 60, pp. 65–75, Jul. 2015.

[66] P. Mattesini *et al.*, "Spectral Doppler Measurements with 2-D Sparse Arrays," in *2018 IEEE International Ultrasonics Symposium (IUS)*, 2018, pp. 1–4.

[67] P. Santos, G. U. Haugen, L. Lovstakken, E. Samset, and J. D'hooge, "Diverging Wave Volumetric Imaging Using Subaperture Beamforming," *IEEE Trans. Ultrason. Ferroelectr. Freq. Control*, vol. 63, no. 12, pp. 2114–2124, Dec. 2016.

[68] M. S. Wigen *et al.*, "4-D Intracardiac Ultrasound Vector Flow Imaging–Feasibility and Comparison to Phase-Contrast MRI," *IEEE Trans. Med. Imaging*, vol. 37, no. 12, pp. 2619–2629, Dec. 2018.

[69] F. Guidi, A. Dallai, E. Boni, A. Ramalli, and P. Tortoli, "Implementation of color-flow plane-wave imaging in real-time," in *2016 IEEE International Ultrasonics Symposium (IUS)*, 2016, pp. 1–4.

[70] K. Ranganathan, M. K. Santy, T. N. Blalock, J. A. Hossack, and W. F. Walker, "Direct sampled I/Q beamforming for compact and very low-cost ultrasound imaging," *IEEE Trans. Ultrason. Ferroelectr. Freq. Control*, vol. 51, no. 9, pp. 1082–1094, Sep. 2004.

[71] A. Østvik, E. Smistad, S. A. Aase, B. O. Haugen, and L. Lovstakken, "Real-Time Standard View Classification in Transthoracic Echocardiography Using Convolutional Neural Networks," *Ultrasound Med. Biol.*, vol. 45, no. 2, pp. 374–384, Feb. 2019.